Aerodynamic Loads on an Aft-Mounted Propeller Induced by the Wing Wake

van Arnhem, Nando; Vos, Roelof; Veldhuis, Leo

DOI
10.2514/6.2019-1093

Publication date
2019

Document Version
Final published version

Published in
AIAA Scitech 2019 Forum

AIAA SciTech Forum
7-11 January 2019, San Diego, California
AIAA Scitech 2019 Forum

10.2514/6.2019-1093

Aerodynamic Loads on an Aft-Mounted Propeller Induced by the Wing Wake

Nando van Arnhem*, Roelof Vos†, and Leo L. M. Veldhuis‡
Delft University of Technology, Delft, 2629 HS, The Netherlands

This paper presents an experimental and numerical study of the aerodynamic in-plane and out-of-plane loads of a propeller which are induced by the wake of an upstream wing impinging on the lower half of the propeller disk. A propeller was installed behind a wing model in a low-speed wind-tunnel and measurements were taken with an external balance and a rotating shaft balance to determine the aerodynamic characteristics of the wing and propeller. The installation of the wing shows negligible changes in propeller thrust coefficient at low advance ratios, while at medium thrust conditions ($C_T \approx 0.3$), the wing shows a small increase in propeller thrust in the order of 1%. The installation of the propeller aft of the wing shows a change on propeller efficiency ranging from $\Delta\eta_p$=–0.01 to +0.04. The location of the wake impingement at the propeller plane is shown to play an important factor for the time averaged and unsteady propeller loads. The radial location where the largest change in load occurs due to wake impingement, coincides with the location of highest propeller loading. A simplified and computationally efficient method is presented for estimation of these unsteady propeller loads in non-uniform inflow. The method shows good agreement for the integral unsteady blade thrust and integral propeller for different wake impingement locations.

Nomenclature

b = Span [m]
B = Number of propeller blades
$c, \bar{c}$ = Chord, mean aerodynamic chord [m]
C_D = Drag coefficient, $\frac{D_w}{q_\infty S_w}$
C_L = Lift coefficient, $\frac{L_w}{q_\infty S_w}$
C_N = Propeller normal-force coefficient, $\frac{N}{\rho_\infty n^2 D^4}$
C_{N_α} = Gradient of normal-force coefficient C_N versus angle of attack curve [rad^{-1}]
C_T = Propeller thrust coefficient, $\frac{T}{\rho_\infty n^2 D^4}$
C'_T = Thrust coefficient of a section, $\frac{T'}{\rho_\infty n^2 D^4}$ [m^{-1}]
D = Diameter [m], drag [N]
J = Advance ratio, $\frac{V_\infty}{nD}$
L = Lift [N]
N = Normal-force [N]
n = Propeller rotational speed [s^{-1}]
p = Observed order of accuracy
P = Shaft power [Watt]
q = Dynamic pressure, $\frac{1}{2}\rho V^2$ [Pa]
Q = Propeller torque [Nm]
R = Propeller radius [m]
S = Area [m^2]
T = Propeller thrust [N]
T' = Thrust on blade section [N · m^{-1}]
T_c = Thrust coefficient, $\frac{T}{\rho_\infty V_\infty^2 D^2}$
u, v, w = Velocity in Cartesian coordinate system [m · s^{-1}]
U_s = Standard deviation of a fit based on observed order of convergence
U_ϕ = Estimated discretization uncertainty
V = Velocity [m · s^{-1}]
x, y, z = Cartesian coordinates [m]
Y', Z' = Force on blade section in y-direction [N · m^{-1}]
Z' = Force on blade section in z-direction [N · m^{-1}]
α = Angle of attack [deg]
η = Efficiency, $\frac{TV_\infty}{P}$
ϵ = Downwash angle [deg]
ρ = Density [kg m^3]
ϕ = Propeller phase angle [deg]

Subscripts
∞ = Freestream
iso = Isolated propeller
p = Propeller
t = Total
w = Wing

Superscripts
* = Based on theoretical order of convergence

*Ph.D. Candidate, Flight Performance and Propulsion Section, Faculty of Aerospace Engineering, N.vanArnhem@tudelft.nl; AIAA member.
†Assistant Professor, Flight Performance and Propulsion Section, Faculty of Aerospace Engineering; Associate Fellow AIAA.
‡Full Professor, Flight Performance and Propulsion Section, Faculty of Aerospace Engineering; AIAA member.

I. Introduction

Because of the inherently high efficiency of turboprop propulsion systems compared to turbofan engines, propellers are an attractive means of propulsion for the next-generation passenger aircraft [1–3]. However, the installation penalty of large diameter propellers and their noise levels induced to the cabin in the propeller plane, makes the wing-mounted propeller configuration less practical. An alternative is to mount the the propellers on pylons or at the aircraft tail, which has the potential to reduce the cabin noise compared to the wing-mounted configuration [2, 4, 5]. Such layout has been investigated in several studies with a focus on design, aerodynamics and performance [2, 6–8]. Recently, the rear mounted propeller is also of interest for distributed propulsion concepts (e.g. in Ref. [9]).

Compared to wing-mounted configurations, the inflow field to the propeller may be less uniform. This inflow is characterized by the wing downwash and, at high angle of attack conditions, also by the wing wake, as illustrated by Fig. 1. When employed in a design, a trade-off is to be made on the propeller location relative to the aircraft center of gravity and wing, which will impact the aircraft's performance. To avoid excessive interaction noise, conceptual design studies (e.g. Ref. [2]) avoid a wing wake impingement on the propeller in normal operating conditions by placing the propeller relatively high compared to the wing. However, at high angle of attack, as sketched in Fig. 1(b), a wake impingement can still occur and increases the propeller thrust and torque locally. As shown in Fig. 1(c), an asymmetric impingement also leads to non-zero inplane forces. These forces directly contribute to the aircraft trim and stability and are especially pronounced for an the aft-mounted location of the propeller. For design purposes, a computationally efficient method is preferred to predict the effect of an asymmetric wake impingement on the propeller in-plane, out-of-plane and moments.

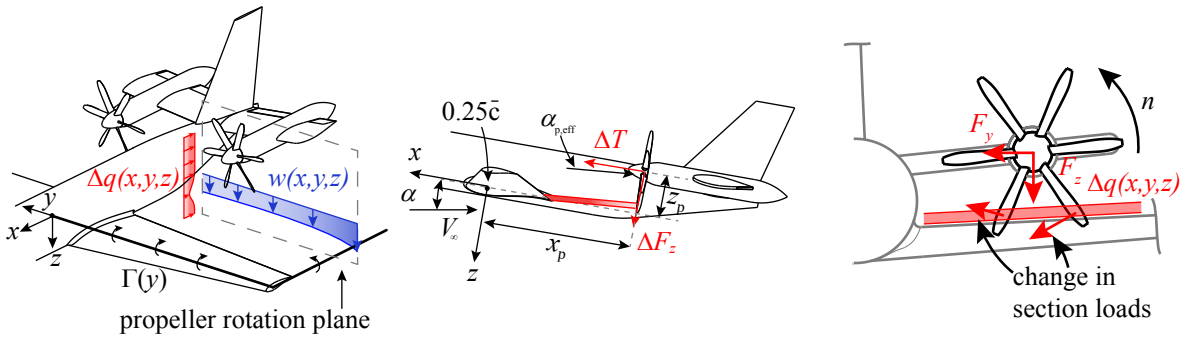

(a) Inflow field to an aft-mounted propeller (b) Wake impingement at high angle of attack (c) In plane forces due to wake impingement

Fig. 1 Schematic of a tail-mounted propeller operating in a downwash and wake field from the main wing. Schematic of in-plane and out-of-plane propeller forces due to non-uniform and asymmetric inflow.

The interaction with an aerodynamic surface upstream of a propeller has been investigated in several studies on traditional pusher configurations. The assessment of increased propeller noise due the impingement of a wake from an upstream wing or pylon are addressed by Refs. [4, 10–14]. In these studies the propeller is positioned relatively close to the trailing edge and the propeller rotation axis is typically aligned with the wing camber line, hence the impingement is close to symmetric and the complete blade encounters the inflow distortion. The studies show that the wake-impingement results in an unsteady propeller loading and changes of the integral loads, both highly depending on the propeller operating condition. The impact of the relative position of the propeller compared to the upstream surface and the in-plane propeller forces are not discussed in detail. The thin wake with a steep velocity profile coming from a pylon generates large suction peaks, primarily in the leading-edge region of the blade. The focus of these studies is on interaction noise as a result of these pressure fluctuations. Compared to a wake from a pylon, the wing wake generally has more momentum loss. However, it has developed downstream by widening and reduction of the velocity gradient, while the integral momentum defect is approximately maintained within a few chords from the wing trailing edge [15]. This results in a relatively larger effect on the average inflow to the propeller, while the unsteady loading is more gradual and a larger area of the propeller disk is encountering the disturbance. For this particular non-uniform inflow, a study of the propeller forces is necessary to estimate the impact on the aircraft stability derivatives and aerodynamic coefficients.

This paper addresses the time-average and time-dependent propeller forces due to wake impingement through a combined experimental and numerical analysis. An experiment was performed on a typical wing–propeller layout featuring a straight wing and two locations were considered relative to the downstream propeller. These experimental

results provide insight in the time-averaged and time-dependent integral propeller forces over a large range of operating conditions. The presented numerical study on a similar geometry consist of two parts. First, full-blade unsteady RANS CFD simulations provide detailed propeller loading distributions which will contribute to the understanding what the influence is of the location of the wake impingement on the propeller disk. In the second part of the numerical study, a simplified method is presented to predict the location of maximum fluctuations, the unsteady load per blade as well as the integral propeller thrust for the non-uniform inflows considered in this paper. These results can be valuable in the assessment of different locations of the propeller relative to a wake inflow.

II. Experimental Setup

This section discusses two experimental setups. The wing–propeller configuration is presented in Section II.A, while a separate isolated propeller experiment was conducted which serves as validation for the numerical simulations of the propeller and is discussed in Section II.B.

A. Wing–Propeller Configuration

The experimental campaign was performed at the Open-Jet Facility (OJF) at Delft University of Technology. The octagonal test section of this low speed open-jet tunnel has a width and height of 2.85m. The wing and propeller model, shown in Fig. 2 (a), were installed on a ground plane flush with the wind tunnel exit and acted as a symmetry plane. The propeller featured a diameter of 0.4064 m and its six blades were set to a blade pitch angle of 45 deg at 70% of the radius. The blade geometry is presented in Li et al. [16]. This rather high blade pitch angle was used to achieve representative T_C and C_T values at high advance ratios, typical for full scale propellers at cruise conditions. The propeller was driven by an TDI 1999A airmotor housed inside a nacelle with a radius of $0.2R$. The nacelle was connected to a straight support strut, as shown in Fig. 2(a). The propeller forces and moments were measured by means of a Rotating Shaft Balance [17]. A time average was taken over 10 seconds and each condition was measured four times.

The selected wing had no taper, sweep and twist and featured a NACA 64_3418 airfoil. The boundary layer on the wing was tripped using zig-zag strip installed on the wing surface at 5% and 10% of the chord on the suction and pressure side of the wing respectively and transition was checked for the considered range of angles of attack. This wing is referred to as the 'smooth wing'. In addition to this smooth wing geometry, additional roughness as shown in Fig. 2(b) was applied on the wing surface to manipulate the wing boundary layer obtain a wing wake with more momentum loss impinging the propeller, while the Reynolds number for the propeller remained unaltered. The selected roughness was sandpaper with an average particle diameter of 425 μm. The constant thickness of the sheets resulted in an increase of maximum thickness-to-chord ratio from 18.0% to 18.8%.

Although the setup is a conceptual representation of the configuration shown in Fig. 1, typical values of wing–propeller spacing and the relative size of the wing for an aft-mounted configuration are used, and were based on Goldsmith [2]. Figure 2(cb) provides an overview of the chosen values. Two z-positions of the wing were considered such that the location of wake impingement could be altered. The two locations were selected as $z_w/R = 0$ and $z_w = -0.74R$, where the former case can be considered as a high-wing configuration (Fig. 2(c)), and the latter represents an aft-mounted propeller configuration featuring a low-wing.

The integral forces generated by the wing were acquired using an external six-component balance, which was mounted on a turntable to change the wing angle of attack about its quarter chord line. For the isolated propeller measurements, the propeller setup was installed on this turntable. For the wing–propeller combination, the propeller rotation axis remained parallel to the freestream flow direction. This means that a positive change in wing angle of attack resulted in a wake impinging more towards the propeller tip. It is noted that when installed on an aircraft, the propeller also is at an angle of attack with the freestream flow, hence the location of wake impingement varies more in the experiment for a given wing lift coefficient.

A freestream velocity of 29 m/s was selected for all measurements and was the maximum achievable value for all test cases. This velocity leads to a wing chord based Reynolds number Re_{c_w} of approximately 500,000. This Reynolds number is significantly lower than the flight regime of a full scale configuration. Hence, both cases with a smooth wing surface and the surface with applied roughness result in a wake characterized by large momentum thickness. This may result in an over-predicted wake effect on the propeller. The propeller was operated at a range of advance ratios J by changing rotational speed. The cases where additional roughness was applied to the wing were limited to $J = 1.0$, 1.6 and 2.4, which correspond to a high thrust coefficient C_T, high efficiency and low thrust coefficient respectively as depicted in Fig. 7.

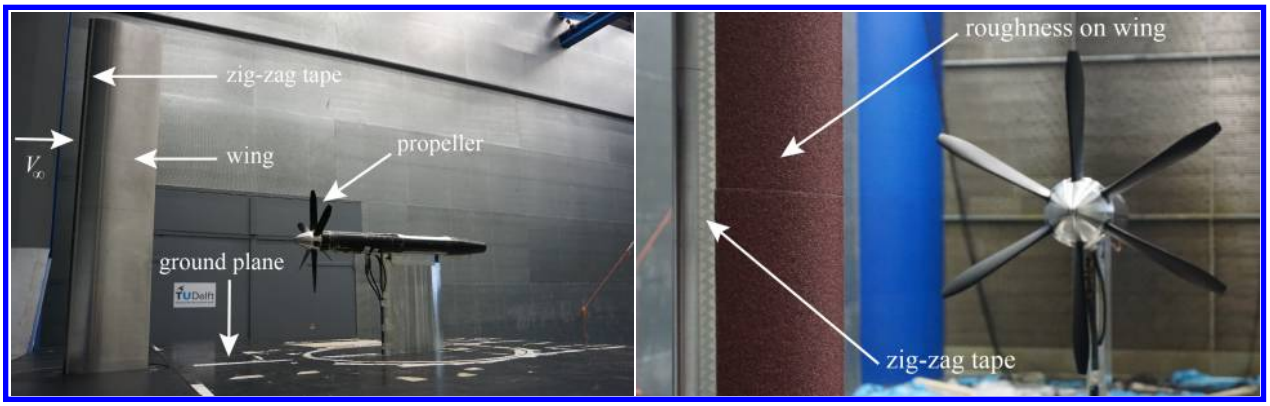

(a) Wing and propeller model installed in the Open Jet Facility

(b) Roughness on wing surface for boundary manipulation

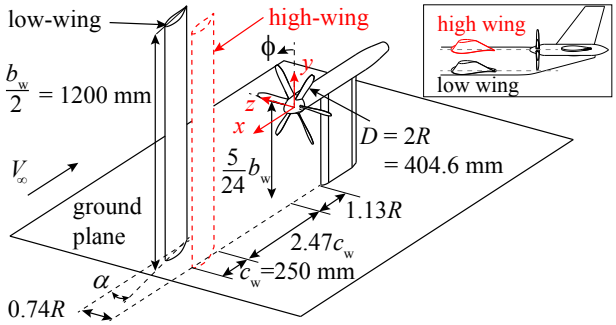

(c) Technical drawing of setup in the Open Jet Facility

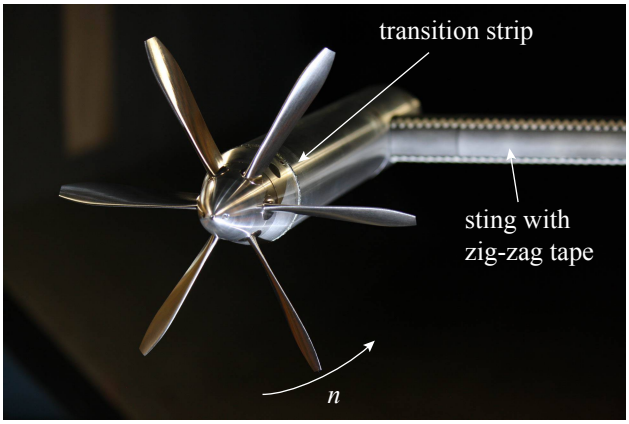

(d) Isolated propeller installed on a sting in the Low Turbulence Tunnel. This is a 1:2 scale version the of propeller in Fig. 2 (a).

Fig. 2 Wing–propeller setup and isolated propeller installed in the Open Jet Facility respectively Low Turbulence Tunnel at Delft University of Technology.

B. Isolated Propeller for Validation

Both flow field and balance measurements were obtained for a 1:2 scaled version of the propeller in the wing–propeller study, shown in Fig. 2 (d), and are used as validation for the computational study discussed in the next section which features this scaled propeller. The minimum trailing edge thickness of the steel blades was maintained at 0.2mm.

The performance of the isolated propeller is characterized by installing it on a nacelle which was mounted on a sting in the center of the wind tunnel section of the Low-Turbulence Tunnel (LTT) at Delft University of Technology, a closed-return low-speed wind tunnel. The drag of the nacelle, spinner and sting are estimated by replacing the propeller with a dummy spinner. Balance measurements were performed at a range of advance ratios at different freestream velocities to determine the dependency of the propeller performance on Reynolds number. A freestream velocity of 40 m/s was selected as baseline and the advance ratio was varied from $J = 2.3$ up to $J = 1.8$. At this velocity, the turbulence level was below 0.1%. Total pressure measurements were taken at $1.1R$ distance from the isolated propeller using a pitot tube.

III. Computational Strategy and Validation

An overview of the computational strategy of the isolated and wing–propeller simulateions is given in Section III.A. The results of the isolated propeller simulation is validated in Section III.B. Section III.C discusses the computationally efficient method to predict the propeller loads due to the wake impingement.

A. Full Blade CFD Simulations

The numerical analyses of the wing–propeller model are performed by solving the RANS equations for compressible flow time-accurately. These full-blade sliding mesh propeller simulations are performed to capture the unsteady nature of the wing–propeller interaction. The isolated propeller simulations are solved in a steady manner using a multi-reference frame approach.

The isolated propeller is solved in a wedge shaped domain depicted in Fig. 3 (a), consisting of subdomains with refined grids. The propeller blades, spinner and nacelle are modeled as no slip walls. Periodic conditions are used on the sides of the wedge, while a pressure inlet, pressure outlet and pressure far-field boundary condition is set on the remaining boundaries. The rotating domain and the adjacent domain capturing the propeller slipstream are coupled by means of interfaces. To maintain consistency, the wing–propeller domain, shown in Fig. 3 (b), contains a copy of the full revolution of the propeller and slipstream domain, matching the mesh of the isolated propeller. A symmetry boundary condition is set on the symmetry plane. A NACA 0015 wing with a semispan equal to three propeller diameters and an aspect ratio of 7.5 is placed in a refined domain upstream of the propeller. This domain is coupled to the rotating propeller domain by means of an interface. Both domains contain refined grids to avoid excessive dissipation of the wing wake and to reduce the interpolation error at the interfaces.

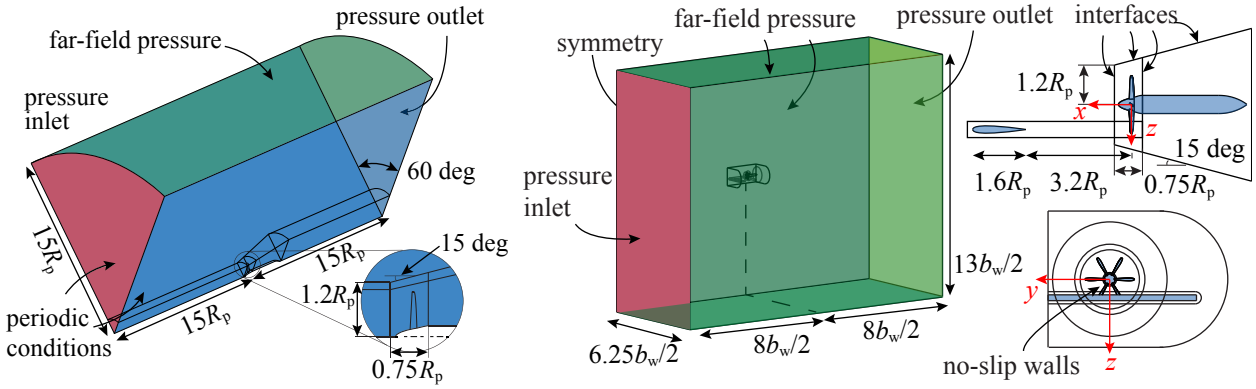

(a) Isolated propeller domain

(b) Wing–propeller domain

Fig. 3 Computational domain and boundary conditions used for the simulations.

ANSYS® Fluent Release 18.1 [18], an unstructured finite volume cell-centered solver, is used to perform the simulations. A second order spacial and temporal discretization is employed, using a coupled pressure-velocity scheme. The sliding mesh simulations are time-accurate, with a time step equivalent to 2 deg propeller rotation with 35 inner iterations. The flow is prescribed to be fully turbulent using the Spalart–Allmaras turbulence model with the strain/vorticity-based production equation, which was shown to compare well with experiments of propeller–wing simulations with similar Reynolds number [19]. A maximum y^+ of 1 is obtained, resulting in a resolved boundary layer. Values for the inlet turbulence quantities are based on the recommendations by Spalart and Rumsey [20], which resulted in an eddy viscosity ratio of 0.21044. Standard sea-level atmospheric conditions are used for the freestream flow. For the equation of state, an ideal gas was assumed and Sutherland's law is used to predict the corresponding dynamic viscosity.

Table 1 Different grids for the isolated propeller simulations

Grid	h_i/h_1	Number of elements
Grid 1	1.00	17,986,198
Grid 2	1.25	9,163,007
Grid 3	1.55	4,841,676
Grid 4	1.87	2,744,493

Table 2 Results of grid study for the isolated propeller. Values are based on grid 3.

	C_T	C_P	max(P_t)	$(T')_{0.85R}$	$(T')_{0.85R}$
p	0.40	1.31	-	-	-
U_s [%]	0.04	0.01	-	-	-
U_s^* [%]	0.06	0.03	0.92	0.17	0.07
$\lvert U_s \rvert$ [%]	0.55	0.91	9.83	0.68	0.24

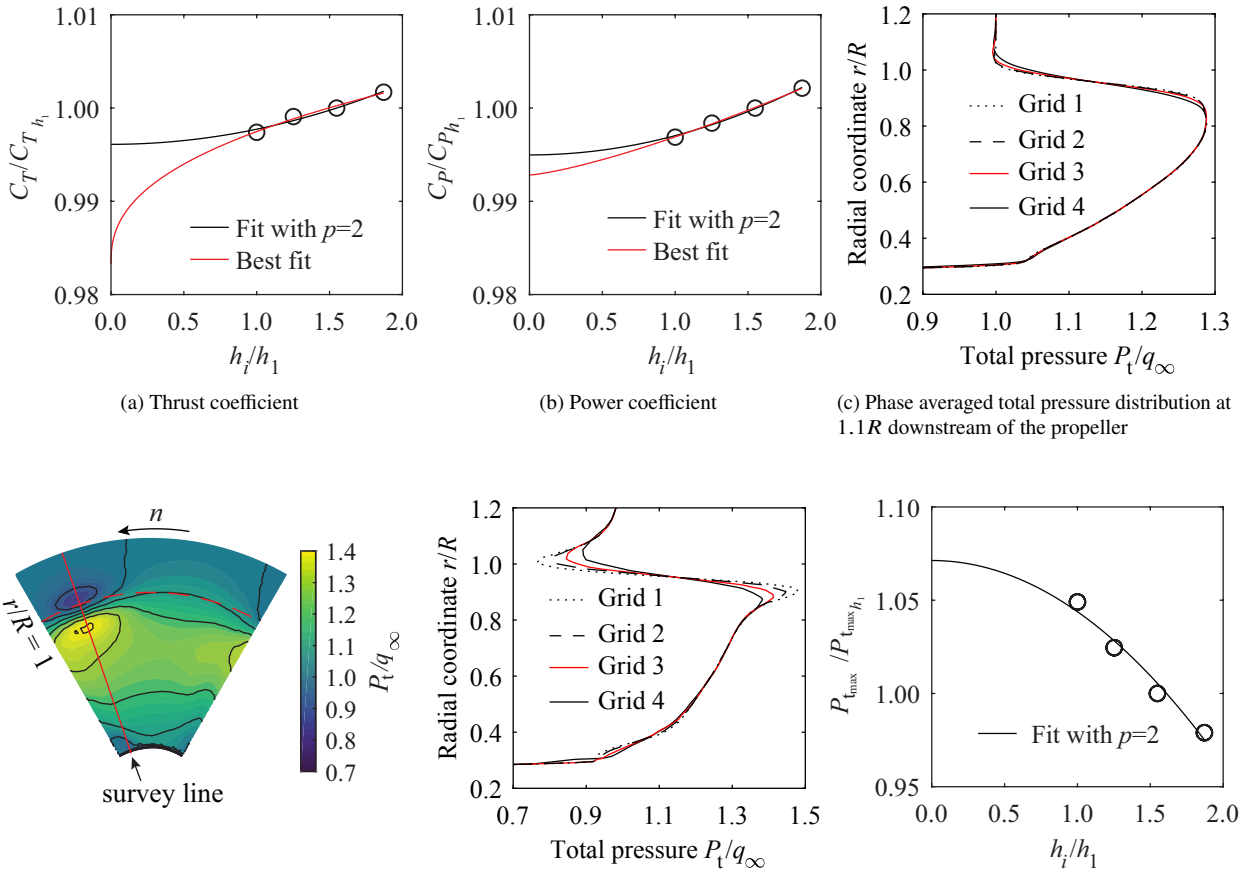

(a) Thrust coefficient

(b) Power coefficient

(c) Phase averaged total pressure distribution at $1.1R$ downstream of the propeller

(d) Total pressure in a plane $1.1R$ downstream of the propeller.

(e) Total pressure distribution along a survey line (defined in Fig. 4(d)) coinciding with the tip vortex

(f) Maximum total pressure in slipstream

Fig. 4 Mesh refinement study for the isolated propeller and isolated wing grids.

The results of four different meshes of the isolated propeller, provided in Table 1, are used to select a grid for the propeller and adjacent slipstream domain. The refinements are varied systematically with same refinement factor for all domains, while the inflation layer which is kept constant. This leads to the refinement factors for the complete domain as listed in Table 1. A least-squares version of the grid convergence index (GCI) as proposed by Eç and Hoekstra [21] is applied to estimate the discretization error, similar to the study in Ref. [19]. The theoretical order of convergence for the selected scheme is close to second order. In Fig. 4(a) and (b) the propeller thrust respectively power coefficients are plotted with respect to the average cell size of grid 1, including a fit of second order and a curve of observed order. Despite the different order of the best fitting curve, due to the low standard deviation (shown in Table 2) of the second order fit is it considered as a sufficiently good curve to estimate the discretization error at $\frac{h_i}{h_1} = 0$. For the integral thrust and power of the propeller, this error is within 1% for grid 3. Figure 4(c) shows the phase averaged total pressure distribution in the slipstream. Between the four meshes, minor differences are observable up to $r/R = 0.8$. In the tip-vortex region, the finest grid shows a slightly larger total pressure gradient, the result of less diffusion with the finer mesh in the slipstream. This is better observable in Fig. 4(e) showing the total pressure along a line coinciding with the propeller tip-vortex. The distribution shows a low dependency on the different grids over the majority of the radius, while a significant reduction in the peak-to-peak total pressure is observed in the tip-vortex, in line with the results in e.g. Ref. [19]. The grid convergence of the peak in total pressure, shown in Fig. 4(f), shows a diverging trend towards the finer grids. However, a fit of theoretical order still leads to good fit with a small fitting error U_s^*. Similarly, the distribution of local thrust shows an oscillatory convergence, while a second order fit still yields acceptable values of standard deviation and estimated discretization error for grid 3. Therefore, grid 3 is selected as a compromise between

computational efficiency and accuracy, as the finer grids only lead to marginal differences in propeller slipstream quantities and integral forces. For this grid, 40% of the elements are located in the propeller blade domain and 37% in the domain of the slipstream. Based on this grid, the full wing–propeller mesh contains 49,120,947 elements for the case $z_w/R = -0.75$, of which 36% is located in domain containing the wing.

B. Validation of Isolated Propeller Simulation

Figure 5(a) shows the experimentally obtained thrust coefficient C_T curves obtained by means of the balance measurements and the integration of total pressure in the propeller slipstream for a range of freestream velocities. In addition, the CFD results are shown. The lowest advance ratio for each freestream velocity corresponds to the maximum operating condition of the electric motors. Similarly to the findings by Bass [22], there is a clear influence of the Reynolds number on C_T, with a significant shift in the C_T curve at $V_\infty = 20m/s$ compared to $50m/s$. For these conditions, the range of Reynolds number based on propeller chord at $r/R = 0.7$ is between 40,000 and 150,000. A two-dimensional viscous-inviscid coupled panel code indicates the presence of laminar separation bubbles for moderate lift coefficients (not shown in this paper) and large regions of laminar flow over the blade airfoils at these low Reynolds numbers resulting in a reduction in lift curve slope and lift coefficient at $\alpha = 0$, explaining the dependency of C_T on V_∞. The total pressure profile measured at $1.1R$ behind the propeller in Fig. 5(b) shows a quite irregular loading distribution at high advance ratios at a radial location with highest loading, which may be the result from laminar separation.

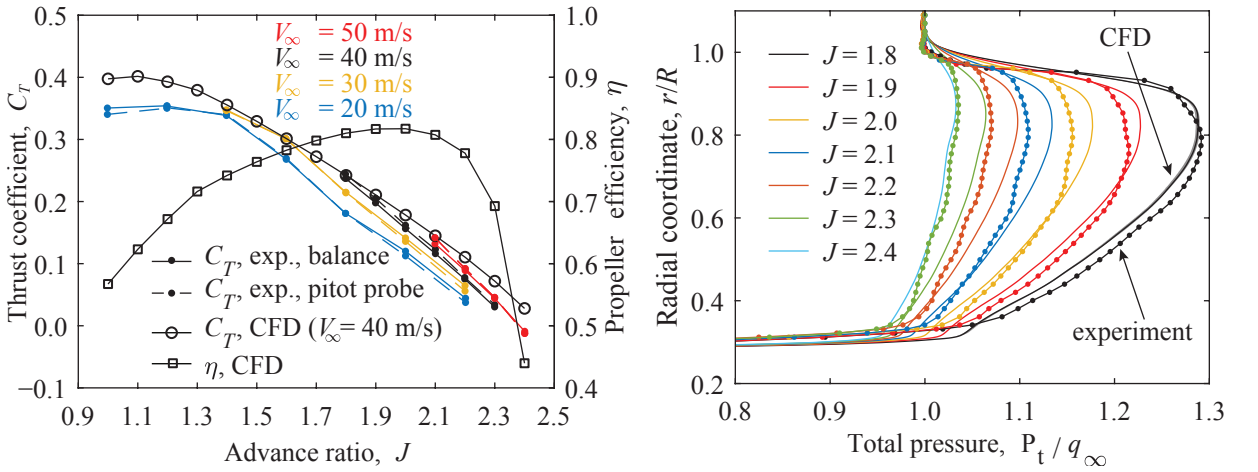

(a) Propeller performance at $\alpha = 0$ deg

(b) Phase averaged total pressure and swirl angle distribution downstream of the propeller at $V\infty = 40$ m/s. Uncertainty is indicated by the shaded area.

Fig. 5 Propeller thrust and flow field obtained in the experiment and computed using CFD at $\alpha = 0$ deg

Compared to the measured thrust coefficient, there is both a shift and a lower slope of the C_T curve computed by CFD at $V_\infty = 40m/s$. From repetitive measurements, it was found that the uncertainty in setting the blade pitch was $+-0.05$ deg. In addition, the maximum fluctuations of the propeller rotational speed as measured by an encoder were 0.1 Hz. As a conservative estimation of these uncertainties, a case with an increase in both blade angle and rotational speed as well as a case with a reduction in both blade angle and rotational speed are plotted for $J = 1.8$ in Fig. 5(b) as well. These uncertainties show to be much smaller than the deviation from the experiment, hence are not likely to be the main factor for the differences with the experiment data. The $C_T - J$ curve intersects at approximately $J = 1.8$ with the experimental data, while the difference at $J = 2.3$ is quite significant. The reduced slope indicates the presence of laminar flow in the experimental test. A better insight in these deviations can be found by comparing the total pressure profile in the slipstream (Fig. 5(b)). The phase averaged total pressure profile by CFD shows quite good agreement with experiment up to $r/R = 0.7$ for the towards the lower advance ratios, while at intermediate advance ratios the deviation is clearly in the highly loaded radial locations. The $J = 2.4$ profile nearly coincides with the $J = 2.3$ profile of the experiment, indicating the offset in sectional lift curve slope at those low Reynolds numbers. The higher pressure losses near the nacelle in the experiment are expected to be the result of the transition strip on the nacelle (Fig. 2(e)). From the figure it becomes clear that the appreciable contraction of the slipstream is slightly under estimated by the numerical

simulations, similarly to the results in e.g. Ref. [23]. Additionally to more diffusion of the propeller tip vortex in the CFD simulations, it is expected that the large flow angles with respect to the probe leads to an inaccuracy of the total pressure measurement in this region. Although there is an offset in $C_T - J$ curve, the phase average of the propeller slipstream is considered acceptable to assess the installed configuration.

C. Simplified Approach to Predict Propeller Loads

Several authors have treated a wake impingement as a local gust to a blade element model, assuming no influence of the gust on adjacent blade sections and from blade to blade. The latter assumption is justified in e.g. Martinez [24] for inflow disturbances that lead to changes in propeller slipstream having a short wavelength compared to the propeller diameter, typically caused by a thin wake. Due to a local increased circulation at location r, the circulation of adjacent sections $r \pm \delta r$ will also increase, which effectively damps the rise in circulation at location r; the disturbance is being spread in radial direction and is especially the case for disturbances which cause a gradual change in load. A disturbance as large as the propeller disk itself is effectively a change in advance ratio for the complete disk. If the rise in local thrust at location r due to a change in local advance ratio ΔJ is assumed to be the same as if this ΔJ applies to the complete propeller disk, then the change in local thrust can be approximated by:

$$\Delta T'(r,\phi) \approx \underbrace{\frac{dT'}{dJ}(r)}_{\text{Property of isolated propeller}} \cdot \underbrace{\Delta J(r,\phi)}_{\text{Non-uniform inflow field}} \tag{1}$$

where $\frac{dT'}{dJ}$ is the sensitivity of the thrust of a blade section to a change in advance ratio for a propeller in uniform inflow and is only a function of radial location. This approach requires only the multiplication of two matrices to find the change in thrust caused by the non uniform inflow. In this approach, it is neglected that the unsteady lift lags behind the instantaneous lift [25]. Therefore in the distribution $\frac{dT'}{dJ}$, it is incorporated that the induced velocities at the encounter of non-uniform inflow have developed instantaneously. The $\frac{dT'}{dJ}$ can be found either experimentally, from CFD or from a blade element model. Figure 6 (a) shows such distribution computed with CFD for the propeller used in the computational study of this paper for a perturbation in velocity and a perturbation in rotational speed. The sensitivity $\frac{dT'}{dJ}$, or equivalently $\frac{dC'_T}{dJ}$, follows the distribution of thrust, with its maximum coinciding at the location of highest load. This is equivalent to the distribution of thrust because the outer regions experience the highest dynamic pressure, and the reduction at the tip is due to tip losses. The shape of the distribution depends therefore on the propeller blade design and number of blades. Effectively, the highest loaded region on a blade is more prone to a disturbance in the inflow field. It is noted that the sensitivity is only valid for small perturbations in the inflow field. The non-linear characteristics of the local sections are not included.

To asses the change in local thrust, the most simple approach is to map the non-uniform inflow on a line at a particular phase angle by representing the blade as a line. However, the finite chord of a blade sweeping through the non-uniform flow means that each part of the chord is exposed to a different inflow. To compensate for this effect, one can determine a weighted average of the projected chord on the non-uniform inflow and represent the blade as a surface. These two representations are illustrated in Fig. 6 (b), while in Fig. 6 (c) an example is depicted of a disturbance distribution and the estimated change in thrust for the two blade representations, where the weighting of the thrust contribution along the chord is taken constant. As expected, the surface representation results in a more smeared change in thrust in radial direction. The two methods applied to a non-uniform flow field will be compared with full blade simulations in Section IV.C.

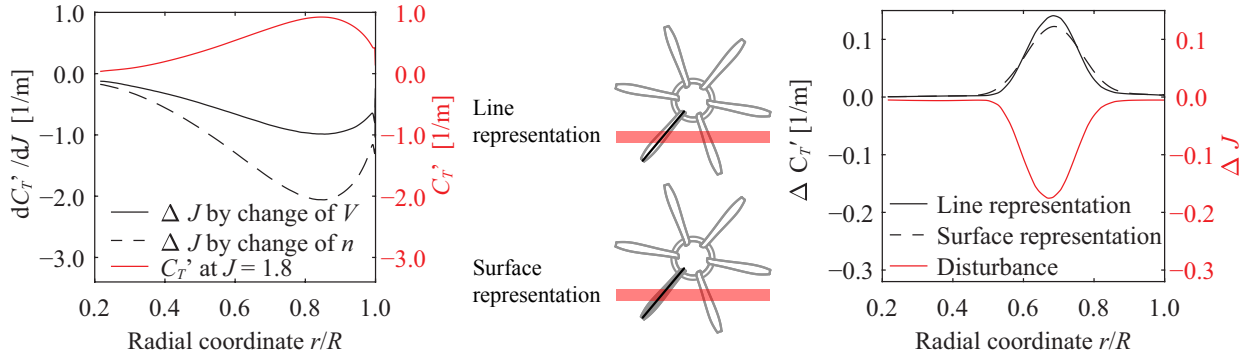

(a) Example of $\frac{dC_T'}{dJ}$ distribution at $J = 1.8$

(b) Line vs. surface encountering a wake

(c) Example of $\Delta C_T'$

Fig. 6 Examples of the radial distributions of changes in thrust of the propeller considered in this paper.

IV. Results

In Section IV.A the experimental results of the wing–propeller aerodynamic interaction are presented. The numerical results to illustrate the changes in local blade loading are presented in Section IV.B. Finally, Section IV.C compares the results of the full blade simulations with the simplified approach.

A. Experimental Results Wing–Propeller Interaction

1. Isolated Propeller and Wing Performance

Figure 7 (a) provides the thrust and torque coefficients and efficiency of the propeller at no angle of attack which serve as baseline. At this blade angle, the maximum efficiency of the propeller is around $J = 1.8$ and corresponds to a high thrust coefficient in the range at which C_T varies linearly with J. At lower advance ratios, it becomes clear that part of the blade experiences stall, while windmilling occurs at an advance ratio of around $J = 2.3$ to 2.4. Because the wing generates a downwash to the propeller, the performance of the isolated propeller at an angle of attack is relevant as reference and is provided in Fig. 7 (b). The relative influence of the asymmetric inflow on the local angle of attack on a blade section vanishes at low advance ratio, hence the variation of C_T with α is small. At high advance ratios there is a consistent increase in C_T with increasing angle of attack. At $J = 1.4$, the trend of increasing C_T with angle of attack stagnates and decreases slightly beyond $\alpha = 10$ deg. It is expected that this is the result of stall on the propeller blades due to the effectively lower J, as indicated by the $C_T - J$ curve in Fig. 7 (a).

The lift and drag coefficients of the wing are presented in Fig. 7 (c) and Fig. 7 (d) respectively for two advance ratios representing the maximum thrust and windmilling conditions. The effect of the applied roughness to the wing is clearly observable as a significant reduction in lift curve slope due to the decambering effect of the thicker boundary layer and a significant shift of the minimum drag coefficient indicating the difference in momentum thickness between the two wings. The propeller is shown to slightly increase the lift curve slope of the wing and postpones the onset of separation to a slightly higher angle of attack. The propeller is also shown to decrease the wing drag coefficient slightly over the complete range of C_L, in particular at higher lift coefficients. Similar results are found by Chao and Zhaoguang [26]. It is expected to be the result of the favourable pressure gradient of the propeller for the wing boundary layer, the slightly higher dynamic pressure upstream of the propeller, a slight offset of lift induced drag and the increase in wing circulation, analogous to over-the-wing propellers (e.g. [27]). The lift-to-drag ratio (not shown) is found to increase over the complete range of lift coefficients, with the maximum L/D value being increased by 4.5%.

2. Downstream Effect of Wing on Propeller Thrust

Figure 8 (a) shows the C_T as function of C_L for the high and low-wing configurations. The wing lift is altered by providing an incidence of the wing with respect to the freestream flow, while the propeller orientation remains fixed. For $J = 1.0$ to 2.0, the low-wing configuration shows a negligible effect of the wing lift on C_T. At the higher lift coefficients, the location of the wing trailing edge and the wing downwash cause the wing wake to go below the propeller disk. The small increase in C_T at lift coefficients larger than $C_L = 0.8$ is therefore dominated by the downwash. This effect diminishes towards the higher advance ratios, in line with the $C_T - \alpha$ curves of the isolated propeller. The high wing

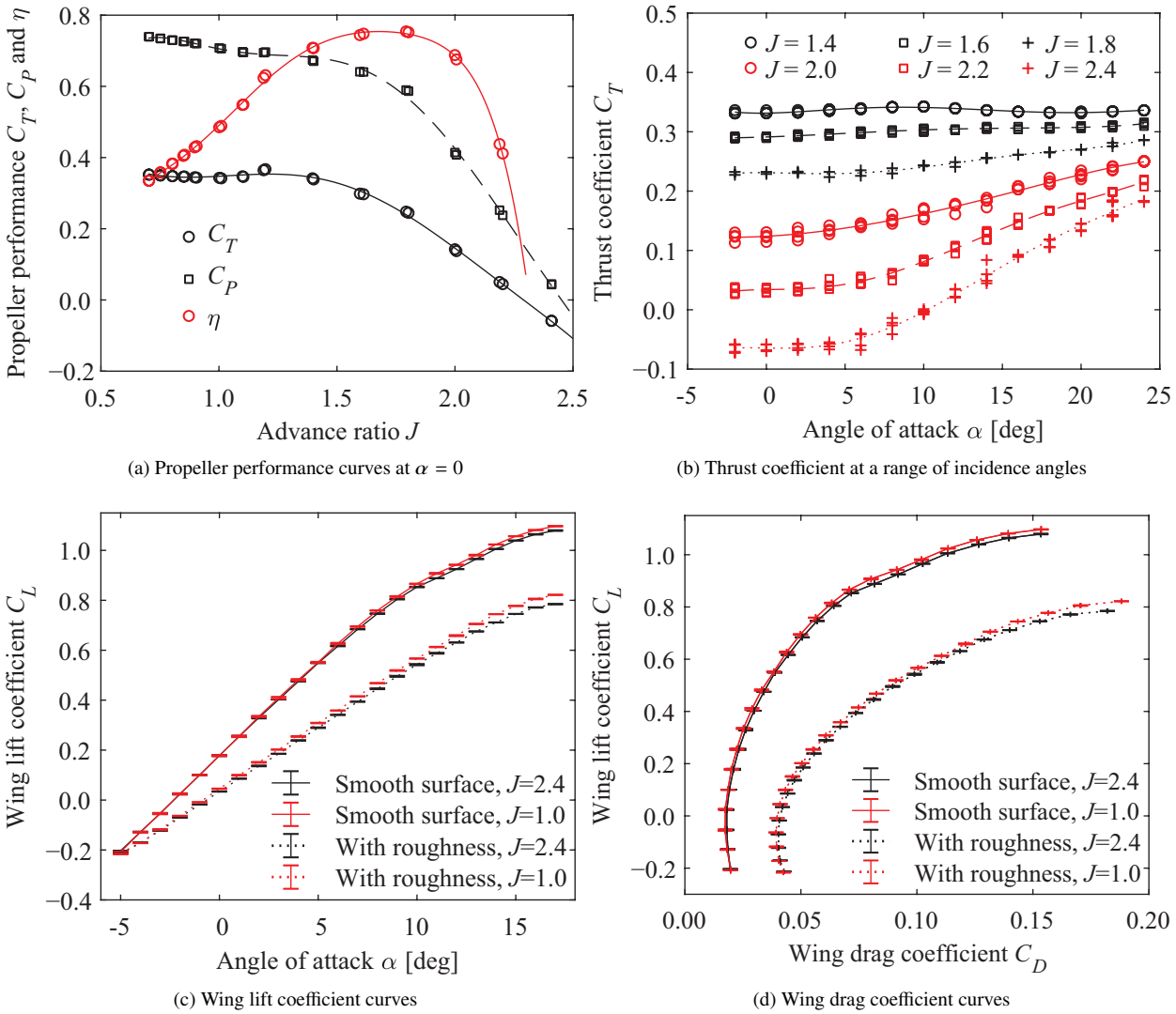

(a) Propeller performance curves at $\alpha = 0$

(b) Thrust coefficient at a range of incidence angles

(c) Wing lift coefficient curves

(d) Wing drag coefficient curves

Fig. 7 In (a) and (b), the isolated propeller performance curves at V_∞= 29 m/s as measured using a rotating shaft balance. In (c) and (d), the integral lift and drag coefficients of the wing at $z_w/R = -0.74$, with and without additional roughness applied. Results for two advance ratios are shown to indicate the upstream effect of the propeller on the wing.

configuration shows similar trends which are more pronounced. Lower advance ratios inherently are less sensitive to the inflow disturbance due to the smaller impact on the angle of attack of the blade sections. In addition, the absence of an increase in C_T at $J = 1.0$ compared to $J = 1.6$ can partially be explained by the isolated propeller $C_T - J$ curve. At $J = 1.0$, the performance curve shows a quite insensitive behaviour to J due to expected blade stall. An impinging wing wake reduces the advance ratio locally even further. At $J = 2.4$ and $J = 1.6$, there is a sudden increase of thrust at a lift coefficient coinciding the deviation from the linear C_L vs. α curve (Fig. 7 (c)) and indicating that the growing wing wake dominates the change in C_T, which is in line with the $C_T - C_D$ curves, where there is especially an increase in thrust for drag coefficients corresponding to the non-linear range of lift. However, the increase in thrust is a combination of the wake-thickening at higher lift coefficients and the different location on the propeller disk of the wake impingement. Figure 6 (a) shows a clear dependency of thrust sensitivity to a change in inflow on the radial location, indicating that the location of wake impingement affects the integral propeller thrust. The limitations of this experimental setup therefore mean that it cannot directly be determined what the relative contribution of these two effects is to the increase in propeller thrust.

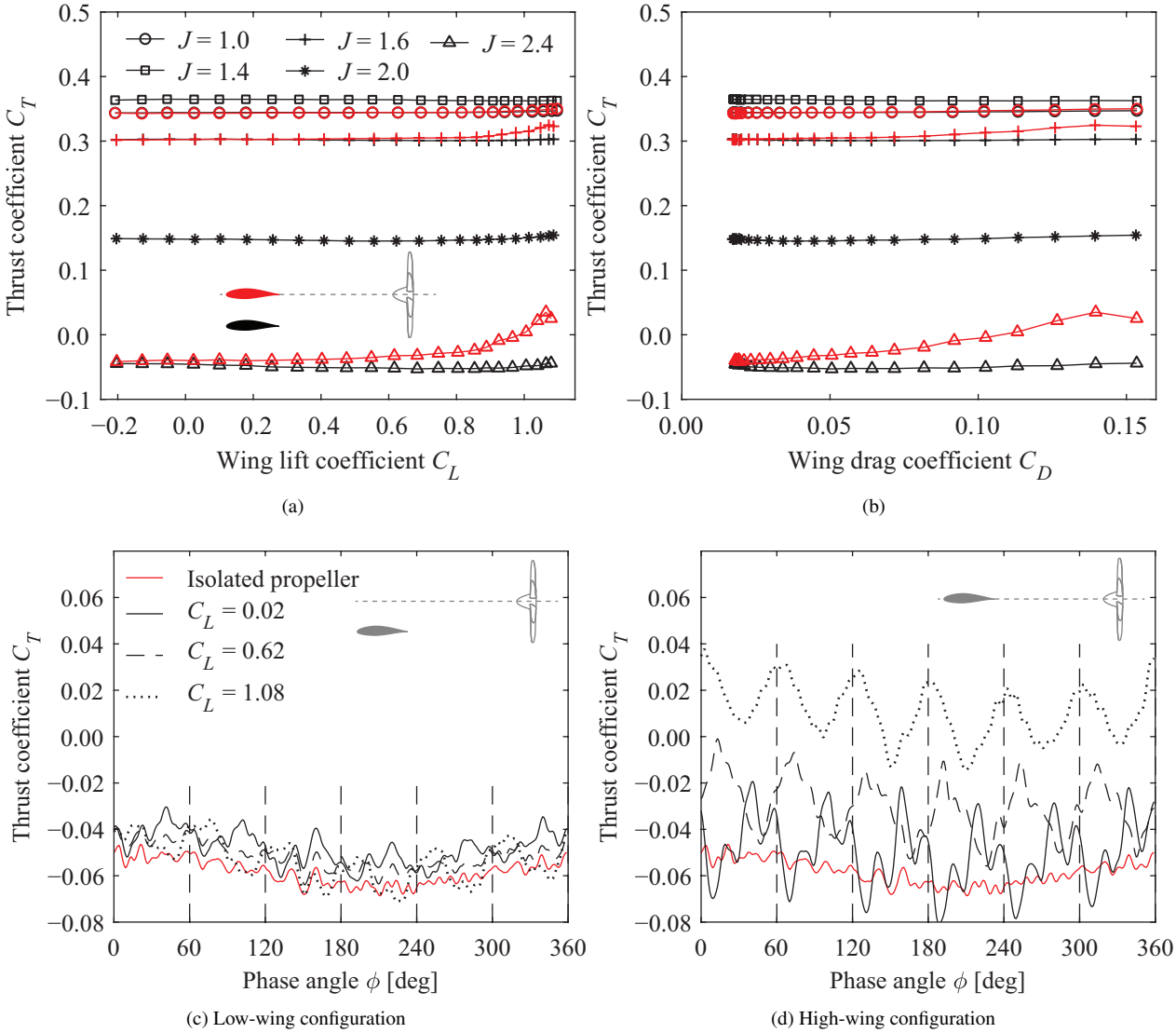

Fig. 8 Thrust coefficient as function of C_L in (a) and C_D in (b). In (c) and (d) the propeller thrust as a function of phase angle at $J = 2.4$. No additional roughness was applied on the wing.

An incidence angle to an isolated propeller leads to a sinusoidal thrust over a full propeller rotation, while a wake entering the propeller disk results locally in a rapid change in propeller thrust. A distinction between the effect of the wing downwash and the impingement of the viscous wake can be made when the propeller thrust is assessed as a function of phase angle. To this end, an phase-averaged thrust is shown in Fig. 8 (a) and (b) for the low, respectively high wing configuration. The results are shown for the isolated propeller and the installed configuration at three different wing lift coefficients at $J = 2.4$ as this is the case with the largest time-average increase in thrust. The curve of the isolated propeller shows a slight dependency on phase angle, characterized by a sinusoidal behaviour. It is expected that this is the result of both the upstream effect of the nacelle support [28] and possibly a slight misalignment of the propeller with the freestream flow. For the installed configuration in Fig. 8 (a), the sinusoidal character of the thrust remains unaltered, indicating the minor influence of the wing downwash on the propeller thrust. With the wing installed, six distinct peaks can be observed. Over a full rotation, each of the six propeller blades experiences the wing wake when the wing produced almost no lift. The shifts of the wave forms for the different lift coefficients are likely due to the different radial position of the wake which impinges on the propeller disk and is discussed in the next section. At the low lift coefficients, it is expected that the wing wake affects the region in which the propeller loading is highest.

At higher lift coefficients, the peaks disappear, in line with the observation that the wing wake goes underneath the propeller disk. The high-wing configuration, Fig. 8 (d) shows a similar trend, where the sinusoidal character of the thrust with a period of one revolution is comparable to the isolated propeller thrust. However, the fluctuations with a period equal to $2\pi/B$ become more distinct. At $C_L = 0.02$, the are small peaks in thrust leading and lagging the highest peak, while these disappear at $C_L = 0.62$ and $C_L = 1.02$. The origin of these additional peaks is not completely understood. The phase shift between the different wing lift and therefore wake location is apparent. The numerical analysis presented in the final paper will give more insight in the influence of the location at which the wake impinges the propeller on the unsteady loading.

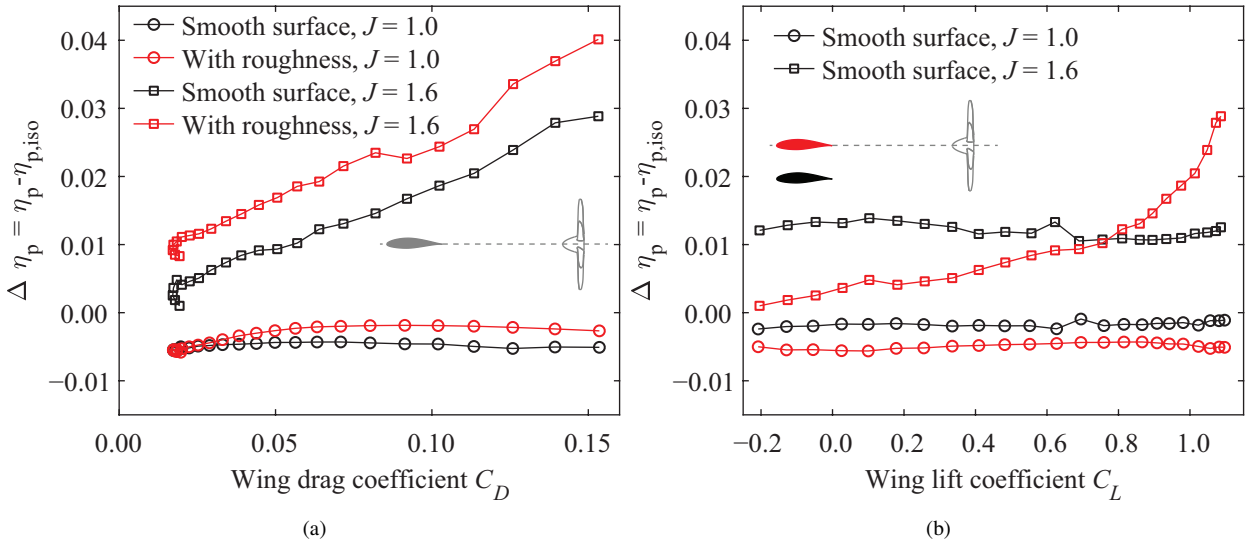

Fig. 9 Change in propeller efficiency by the installation of the wing. In (a) the effect of added roughness is highlighted and in (b) the effect of wing position can be observed.

In addition to the change in propeller thrust, the effect of the upstream wing on the propeller efficiency is a relevant quantity to assess as it directly impacts the aircraft's performance. The non-uniformity of the inflow produced by the wing distorts the propeller loading and hence the propeller efficiency may deviate from the propeller in uniform inflow, a condition for which the propeller is typically designed for. Two factors influencing the propeller efficiency for a given blade pitch angle are the advance ratio and the magnitude of the axial inflow velocity to the propeller disk. Both factors are influenced by the wing wake and downwash, as it reduces both average advance ratio and the average inflow velocity compared to freestream conditions. To this end, it is of interest to compare the propeller loading for the configurations where additional roughness was applied to the wing surface. The change in propeller efficiency as function of wing drag coefficient is shown in Fig. 9 (a) for two advance ratios for the high-wing configuration. At an advance ratio of $J = 1.6$, considered to be a typical cruise condition (Fig. 7 (a)), the propeller efficiency is shown to increase from a small positive value to a $\Delta\eta_p = 0.03$ for the smooth wing model. For the same wing drag coefficient, the $\Delta\eta_p$ for the wing with roughness is shifted and shows values between $\Delta\eta_p = 0.01$ up to $\Delta\eta_p = 0.04$. The increase in propeller efficiency defined relative to V_∞ is analogous to the higher thrust-to-power ratios found in boundary layer ingestion studies, e.g. Ref. [29]. At $J = 1.0$, a condition where part of the propeller blades experience stall, the wing installation results in a reduction of propeller efficiency in the order of $\Delta\eta_p = -0.005$ and is not varying significantly with C_D. It is expected that the efficiency gain of the lower inflow velocity due to the wake is being off-set by locally more separated flow. The difference of the high and low-wing configuration without applied roughness is shown in Fig. 9 (b). The figure indicates a rather insensitive change in propeller efficiency with C_L for the low-wing configuration, while the high-wing shows a monotonous increase in $\Delta\eta_p$. This indicates that the location at which the wake impinges the propeller disk is expected to be a key factor on the propeller efficiency. At a typical cruise lift coefficient of around $C_L = 0.6$, the wing installation shows that the propeller efficiency is increased by $\Delta\eta_p = 0.01$.

B. Full Blade CFD Analysis of Wing Wake Impingement

In this section the full blade CFD simulations as described in Section III.A are discussed which provide more detailed force distributions per blade to determine which regions of the blade are most affected by a wake impingement.

Figure 10 shows the wing wake at the propeller plane for different wing trailing edge–propeller spacings. A spacing of $3.2R$ is selected as baseline case. At this location, the maximum velocity defect is 10% of the freestream flow, equivalent to a maximum $\Delta J = 0.18$ for the reference propeller operating condition of $J = 1.8$. The velocity profiles show that away from the viscous region that the velocity has not fully developed to freestream values due to the presence of the upstream wing. Based on the total pressure profile, the boundary layer thickness of the reference case is $0.20R$ with the edge defined as $0.99^2 P_{t_\infty}$.

The three considered wing locations at $J = 1.8$ are $z_w/R = -0.50, -0.75, -1.00$. The propeller thrust distributions for these wake impingement locations are shown in Fig. 11 (a). The distribution is determined by integrating the pressure and shear stress along the chord at each phase angle to determine the local section thrust. For the $z_w/R = -0.50$ case there are two distinct regions with increased thrust, while at $z_w/R = -0.75$ there is a quite gradual increase of thrust at the location of wake impingement. Azimuthal variations up to 10% of the local thrust are observed for these two cases. The case where the wake is impinging the propeller tip shows little azimuthal variation in thrust. A better insight is gained by plotting the difference with the isolated propeller thrust distribution, shown in Fig. 11 (b), with the red dashed line indicating the blade section with highest thrust in isolated conditions. The increase in thrust for both $z_w/R = -0.50$ and $z_w/R = -0.75$ occurs at a phase angle at which the highest propeller load encounters the wing wake. This is in line with the distribution in Fig. 6(a). Figure 6(a) also shows only a moderate sensitivity of the thrust to a change in advance ratio toward the blade tip, hence the relatively small change in thrust for the $z_w/R = -1.00$ case in Fig. 11 (b). By integrating the thrust distribution for one blade at each phase angle, shown in Fig. 11(c), the maximum deviations to isolated conditions are 3 to 8%. For the wake impinging near the blade tip, there is a one-per-revolution thrust increment. At $z_w/R = -0.50$, there is first a peak in blade thrust at $\phi = 130$ deg, then a reduction followed by a higher second peak. It is expected that the second peak is higher due to the thrust enhancement around $\phi = 180$ deg at which the circulation has already developed. The apparent sinusoidal thrust with a period equal to one revolution is expected to be a combination of two effects. When a blade is advancing towards the wake, the blade which already encountered the wake induces axial velocity on this subsequent blade. This results in a reduction in the local angle of attack of the blade advancing towards the wake, hence, a small decrease in thrust at these phase angles can be expected. In addition, the propeller is found to have a small upstream effect to the wing by introducing a positive angle of attack, which leads to a non-zero wing lift and therefore a downwash to the propeller. This downwash leads to a typical sinusoidal blade forcing.

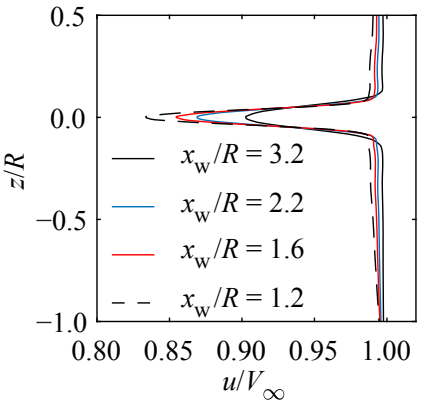

Fig. 10 Wake profile of different trailing edge–propeller spacings.

The integral thrust of the propeller is depicted in Fig. 11 (d), showing fluctuations around 1% of the propeller thrust at the blade passing frequency. At a blade phase angle of $\phi = 0$ deg, both the $z_w/R = -0.50$ and $z_w/R = -1.00$ show the maximum propeller thrust, coinciding with the phase angle at which the blades encountering the wake. At $z_w/R = -0.75$, this is the case for $\phi = \pm 30$ deg, explaining the phase shift of the integral propeller thrust. A similar phase shift between the different wake impingement locations is also observed in the experimental results in Fig. 8 (d). The torque, also depicted in Fig. 11 (d), is shown to follow the same trend as the thrust. The smaller increase in thrust than torque indicates in a higher propeller efficiency, equivalent boundary layer or wake ingesting propellers. This figure shows that in case of a wake impingement, no significant degradation of propeller performance is expected.

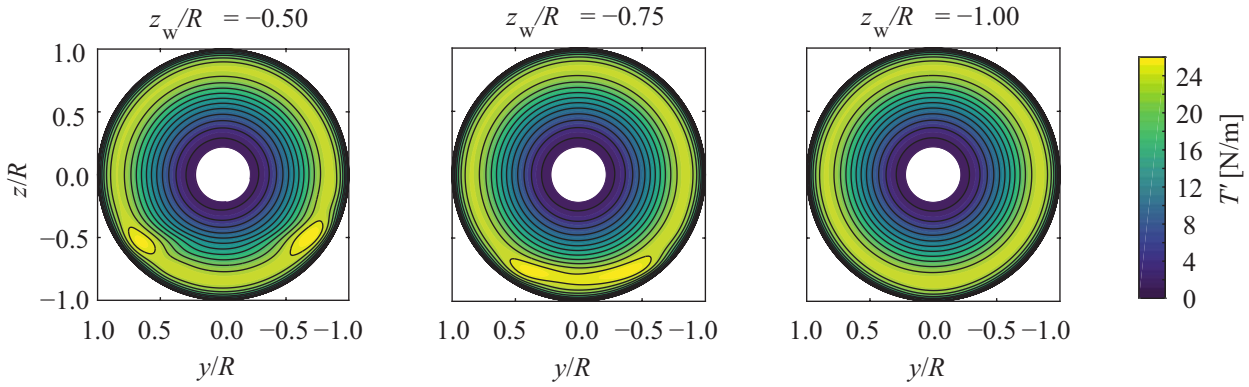

(a) Local blade thrust

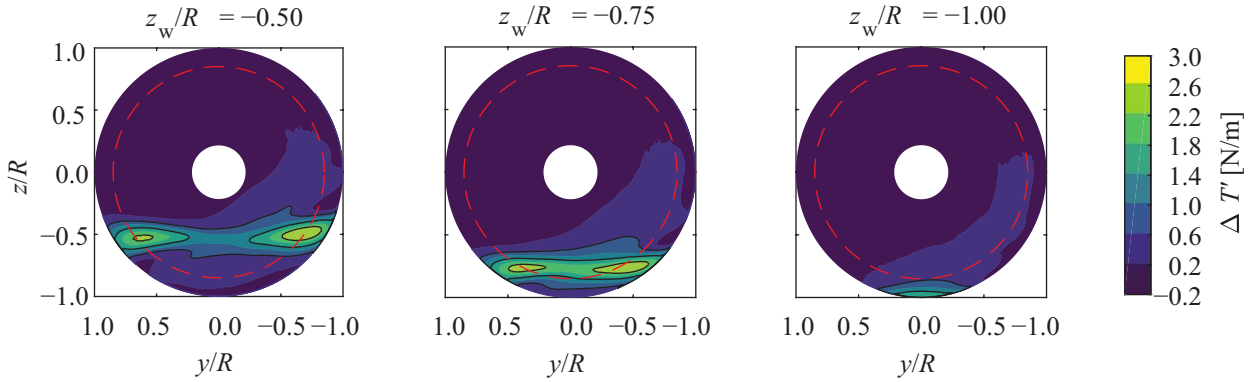

(b) Change in local blade thrust

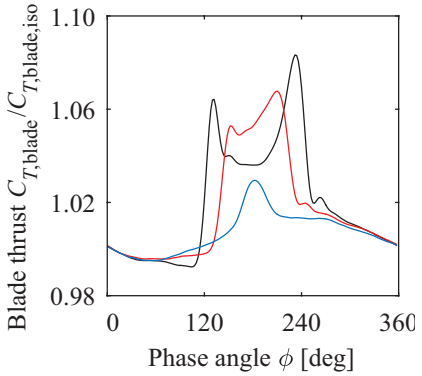

(c) Thrust of one blade

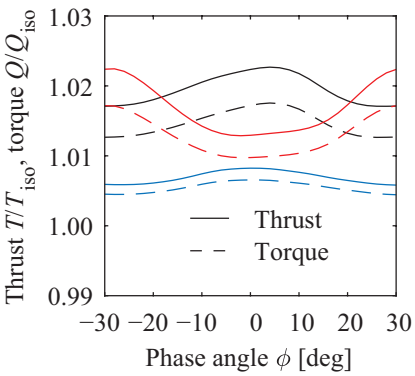

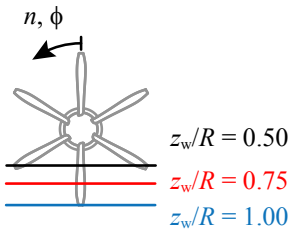

(d) Integral propeller thrust, torque

Fig. 11 Blade thrust distributions at three wing locations with respect to the propeller with a wing trailing edge–propeller spacing of $3.2R$ at $J = 1.8$ and $\alpha = 0$ deg, computed by the full blade CFD simulations.

In addition to changes in propeller thrust, the change of the in-plane forces are an important aspect for the tailmounted propeller configuration. In increment of thrust and therefore torque that arises from an asymmetric wake impingement lead to a net side force, while a torque distribution that is not symmetric with the $x-z$ plane results in a net normal force. The distribution of these in-plane forces are shown in Fig. 12(a) and (b) for the side force coefficient in y-direction and normal force z-direction respectively. The largest increment in thrust for $z_w/R = -0.50$, occurs relatively close to the propeller axis, hence the additional torque is limited. Therefore the largest local side force on a blade section is observed for $z_w/R = -0.75$, while the impingement at the blade tip at $z_w/R = -1.00$ shows only small increment in side force. Although the maximum sideforce acting on one blade (depicted in Fig. 13(a)) occurs for the $z_w/R = -0.75$ case, the integral of the six blades show a marginally larger side force for $z_w/R = -0.50$ due the bigger segment of the disk which is encountering the wing wake. For all wake impingement locations the side force is positive and do not exceed 2% of the propeller thrust. The normal force in z-direction, also shown in Fig. 13(a), is on average slightly negative and is the result of the asymmetry of this force distribution depicted in 12(b). The higher second peak of thrust and torque when the blade tip is encountering the wake for the second time in a revolution results in a net force on the propeller in negative z-direction. To put the magnitude of these in plane forces in perspective, one can compare them to the normal force arising from an angle of attack. The time average of the gradient of normal force with angle of attack C_{N_α} at $J = 1.8$ was found to be 0.59 rad^{-1} computed at $\alpha = 5$ deg and is comparable with the value of 0.63 rad^{-1} estimated by the method of de Young [30]. A side force of 1% of the isolated thrust is equivalent to a propeller at 0.25 deg angle of attack and shows that these in plane forces are small. Practically, for an aft-location of the propeller in a tail mounted configuration, these inplane forces lead to a yawing and pitching moment, but an equilibrium will be found at a small different yaw and pitch angle. These forces contribute to a different trim attitude, rather than altering the longitudinal and lateral stability significantly.

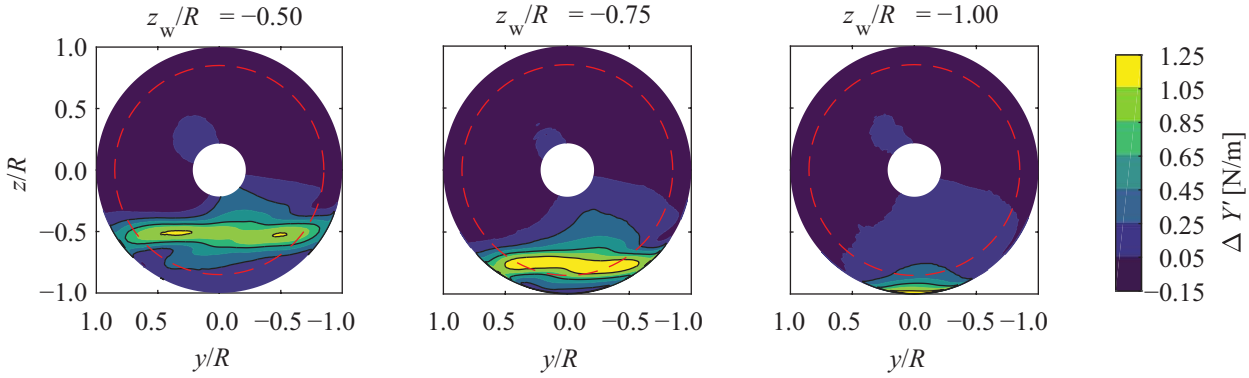

(a) Change in local blade side and normal forces

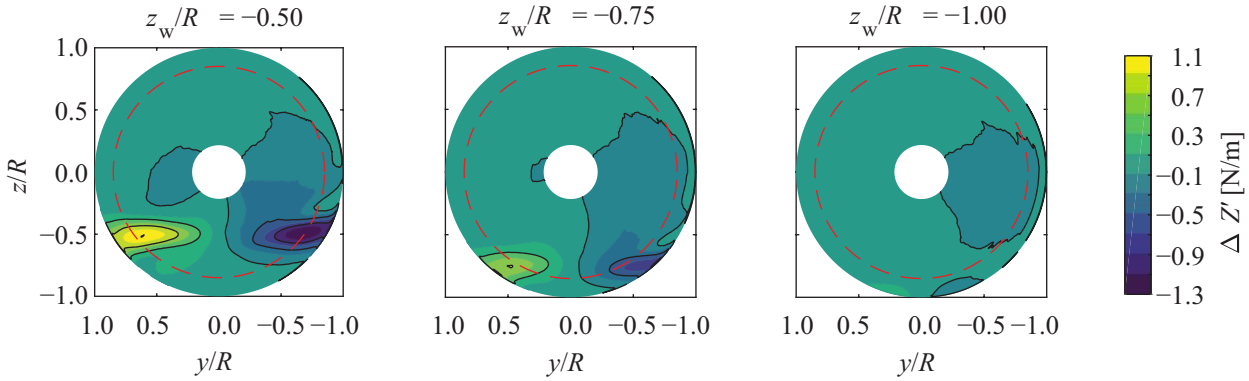

(b) Change in local blade side and normal forces

Fig. 12 Blade in-plane force and moment distributions at three wing locations with respect to the propeller with a wing trailing edge–propeller spacing of 3.2R at $J = 1.8$ and $\alpha = 0$ deg, computed by the full blade CFD simulations.

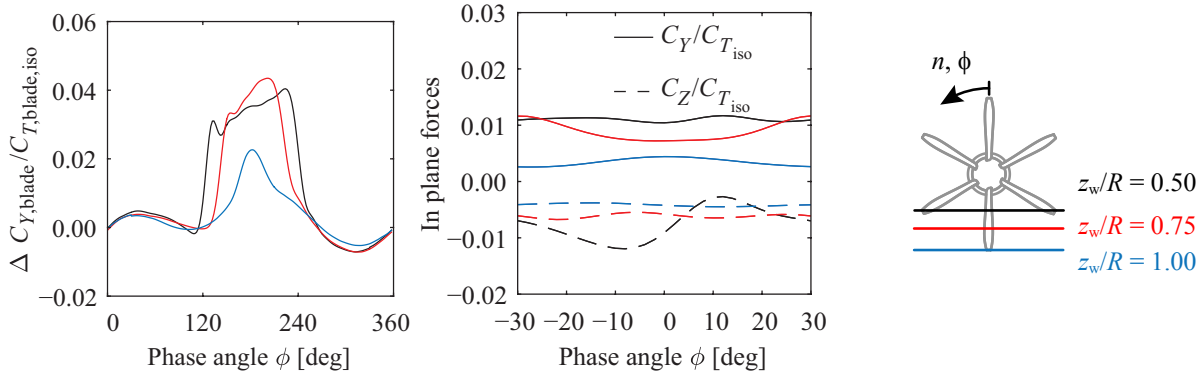

(a) Difference in blade side force

(b) Propeller in-plane forces

Fig. 13 Blade in-plane force distributions at three wing locations with respect to the propeller with a wing trailing edge–propeller spacing of 3.2R at $J = 1.8$ and $\alpha = 0$ deg, computed by the full blade CFD simulations.

C. Estimation of Unsteady Propeller Load Using a Simplified Approach

In Section III.C an approach is presented to estimate the local blade forces due to a non-uniform inflow, based on the sensitivity of the blade sections of a propeller in uniform inflow and the non-uniform inflow which is not altered by the propeller installation. In this section the predicted force distributions are compared with the results obtained from the full blade simulations.

First, a comparison is made between the representation of the blade as a line or a surface sweeping through the non-uniform inflow. The change in local thrust distribution is shown in Figure 14(a) for $z_w/R = 0.50$ as for this case local changes in thrust are more pronounced than the other considered wing locations. The line model does capture the location of maximum increment in thrust quite well, although there is a significant overprediction of the local thrust and the area of the increased thrust exactly follows the wake inflow. In Fig. 6 (c) the difference is highlighted in section thrust computed by a line and a surface that equally extends in both chordwise directions. The line model concentrates the increment in load only to the region of non-uniform. Describing the blade as a quarter chord line with a chord approximately equal to the projected area of the blade, the distribution in thrust is more smeared and is no longer symmetric, as shown in Fig. 14(a). The magnitude of the thrust increment is still overpredicted, but the distribution of $\Delta dT/r$ is close to the full blade solution. It is also observed that the instantaneous thrust of the surface representation is not as smeared in radial and azimuthal direction compared to the full blade solution. This means that although there is a local overprediction of the thrust, the integral blade load is not necessarily overpredicted with by the same factor. The estimated integral blade loads are compared in Figs. 14(b) through (d) for different wing locations by integrating $\Delta dT/r$ for each phase angle. The curves show that the phase angle as well as the magnitude corresponding with the highest load of the full blade simulation are predicted well by the simplified approach. The sinusoidal behaviour of the thrust for all three wing locations was noted as the upstream effect of the propeller on the wing in the previous section. This effect is not included in the simplified approach, hence the difference with the full blade simulation outside the wake region. To indicate its impact on the rest of the distribution, a sinusoid is added to the estimated distribution, also depicted in Figs. 14(b) through (d). Especially for the case where the wing wake is impinging at the tip, this yields to almost an exact match with the full blade simulation. The slight underprediction of the blade loading is expected to be caused by the additional wake inflow due to the pressure field induced by the propeller. For the estimated curve, the inflow is not corrected for the upstream effect. For the other two cases, there is an overprediction of the blade load especially at the peaks.

The change in integral load of the propeller compared to isolated condition is presented in Figs. 14(e) through (g). The change in thrust as a function of wing location is a smooth curve with a relatively constant maximum between $z_w/R = -0.3$ to 0.6. The largest gradient occurs around $z_w/R = -0.75$ where the blade sections most sensitive to a inflow disturbance contribute to the thrust increment. The estimated curves follow the trend of the full blade simulation well, although the overprediction of propeller thrust compared to full blade simulations is 10%. As expected, the estimation model predicts no change in propeller normal force due to the symmetry of the distribution.

It is noted that the computational time of the simplified approach compared to the full blade simulations is extremely reduced. While the full blade simulations presented in this paper required 4,500 CPU hours for each point, the data

points of the curves presented in Figs. 14(e) through (g) were computed within seconds, excluding the computation of the non-uniform inflow field and the sensitivity distributions. This makes the simplified method an attractive method for design purposes where the disturbance of the inflow field is moderate.

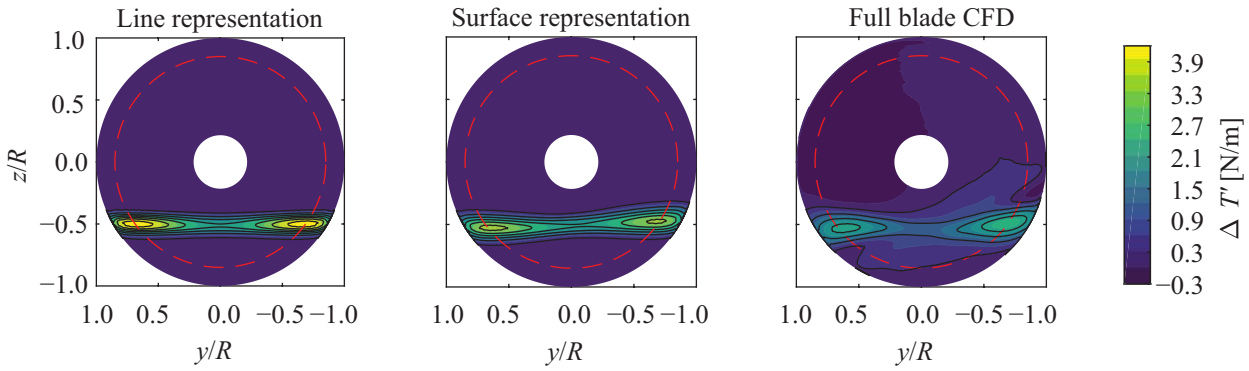

(a) Estimated change in thrust due to wake impingement with $z_w/R = -0.50$

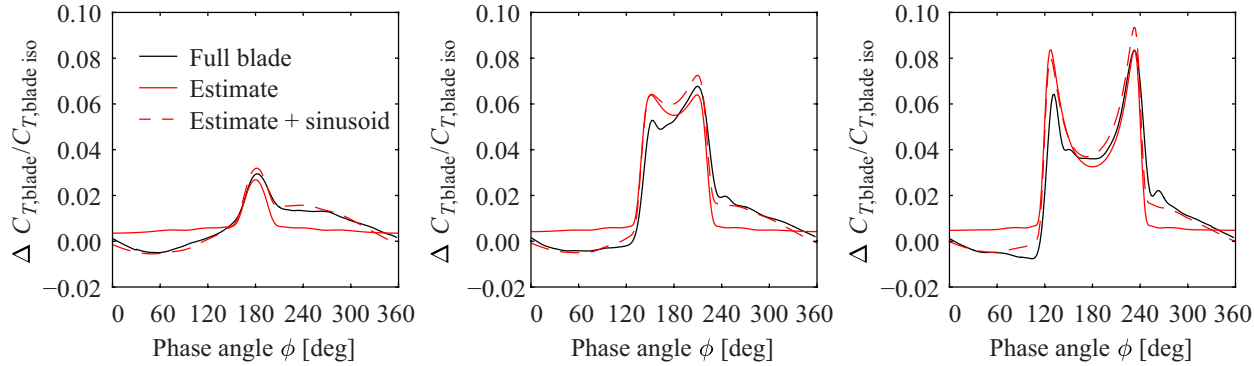

(b) Wing $z_w/R = -1.00$ (c) Wing $z_w/R = -0.75$ (d) Wing $z_w/R = -0.50$

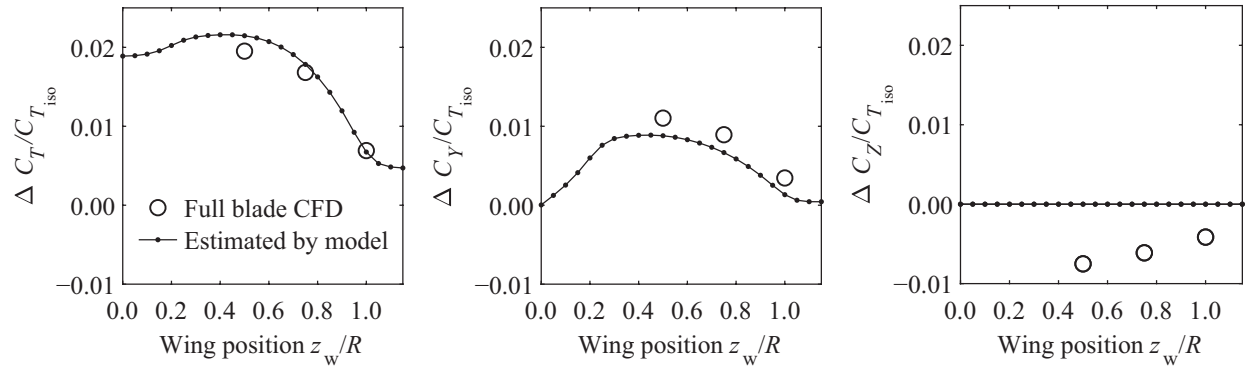

(e) Change in propeller thrust (f) Change in propeller side force (g) Change in propeller normal force

Fig. 14 Comparison of full blade simulation to the simplified approach to predict blade loadings with a wing trailing edge–propeller spacing of 3.2R at $J = 1.8$ and $\alpha = 0$ deg.

V. Conclusions

This paper presents an experimental and numerical study of the propeller forces due to an asymmetric impingement of a wake. The following conclusions are formulated.

The installation of an upstream wing in a low-wing configuration shows negligible changes in propeller thrust coefficient at low advance ratios. At medium thrust conditions ($C_T = 0.3$), the wing shows a small increase in propeller thrust in the order of $\Delta C_T = 0.01$. A high-wing configuration where the propeller is approximately aligned with the wing chord, shows the largest effect on propeller thrust, observed in both time-average and time-dependent propeller loading. At a high advance ratio of $J = 2.4$, the installation of the high-wing results in a change in C_T from –0.045 to 0.03. The wake impingement is the dominating factor in changing the propeller thrust and the wing induced downwash is a secondary factor. This is confirmed by the distinct loading pattern observed in the time-dependent integral thrust values, with an increase in thrust at the phase angle at which the wing wake impinges on the propeller blades.

From the full-blade unsteady RANS simulations it is found that the largest increment in propeller thrust coincides with the radial locations having the largest thrust in isolated conditions, around $r/R = 0.85$. This is analogous to the largest increase in section thrust observed on an isolated propeller subject to a small change in advance ratio. The larger sensitivity to the non-uniform inflow at these radial location results in a two-per-revolution blade thrust increment if the wake impinges at a location spanning from the hub towards the highest loaded blade region, while a wake impingement near the tip results in a one-per-revolution thrust increment. The maximum changes in integral out-of-plane and in-plane forces occur when a wake impinges from in the region spanning from the hub up to 60% of the radius.

A wake with a maximum velocity defect of 10% of the freestream flow results in deviations from isolated blade thrust in the order of 8%, while the integral thrust is increased in the order of 2%. In-plane forces are found up to 1% of the isolated thrust and are equivalent to a propeller at 0.10 to 0.25 deg angle of side slip or angle of attack. These in-plane forces lead to a small change in trim attitude.

A simplified approach is presented to estimate the propeller load distribution by the multiplication of the distribution force-to-advance ratio sensitivity with the non-uniform inflow field. A representation of the blade as a surface sweeping through the non-uniform field is found to overpredict maximum section thrust up to 30%. However, it is found that the distribution of thrust is more smeared in azimuthal direction. This yields that the estimated integral blade load as function of phase angle is in good agreement with the full blade simulations for the considered wake impingement locations. The significant benefit in terms of computational efficiency compared to full blade CFD simulations makes the simplified method an attractive approach for design purposes which are an opportunity for future studies.

Acknowledgments

The authors would like to thank Peter den Dulk and Ed Roessen from the DEMO organisation at Delft University of Technology for the manufacturing of part of the hardware for the experimental campaigns. Furthermore, the help of Tom Stokkermans, Tomas Sinnige and Reynard de Vries to assist with the setup is much appreciated.

References

[1] Whitlow, J. B., and Sievers, G. K., "Fuel Savings Potential of the NASA Advanced Turboprop Program," Tech. Rep. TM-83736, NASA, 1984.

[2] Goldsmith, I. M., "A Study to Define the Research and Technology Requirements for Advanced Turbo/Propfan Transport Aircraft," Tech. Rep. CR-166138, NASA, 1981.

[3] Sullivan, W. E., Turnberg, J. E., and Violette, J. A., "Large-Scale Advanced Prop-Fan Blade Design," Tech. Rep. CR-174790, NASA, 1984.

[4] Neuwerth, G., Lölgen, Th., and Staufenbiel, R., "Increased noise emission of propellers and propfans due to pusher installation," *17th ICAS Congress*, Vol. 1, 1990.

[5] Boctor, M.L., Clay, C.W. and Watson, C.F., "An Analysis of Prop-Fan Airframe Aerodynamic Integration," Tech. Rep. CR 152186, NASA, 1978.

[6] Schouten, T., R., Hoogreef, M. F. M., and Vos, R., "Effect of Propeller Installation on Performance Indicators of Regional Turboprop Aircraft," *AIAA Science and Technology Forum and Exposition*, 2019.

[7] Applin, Z. T., and Coe, P. L., Jr, "Low-Speed Stability and Control Characteristics of a Transport Model with Aft-Fuselage-Mounted Advanced Turboprops," Tech. Rep. NT-2535, NASA, 1986.

[8] Ridder, S.-O., "Wind Tunnel of a Twin, Rear Propeller Transport Aircraft Configuration at Low Speeds," *14th ICAS Congress*, Vol. 2, 1984, pp. 644–654.

[9] de Vries, R., Hoogreef, M. F. M., Vos, R. and Veldhuis, L. L. M., "Preliminary Sizing of a Hybrid-Electric Passenger Aircraft Featuring Over-the-Wing Distributed-Propulsion," *AIAA Science and Technology Forum and Exposition*, 2019.

[10] Sinnige, T., Ragni, D., Malgoezar, A. M. N., Eitelberg, G., and Veldhuis, L. M. M., "APIAN-INF: an aerodynamic and aeroacoustic investigation of pylon-interaction effects for pusher propellers," *CEAS Aeronautical Journal*, 2017. doi:10.1007/s13272-017-0247-2.

[11] Sinnige, T., Ragni, D., Eitelberg, G., and Veldhuis, L. M. M., "Mitigation of Pusher-Propeller Installation Effects by Pylon Trailing-Edge Blowing," *Journal of Aircraft*, Vol. 54, No. 1, 2017, pp. 292–300. doi:10.2514/1.C034000.

[12] Soderman, P. T., and Horne, W. C.,, "Acoustic and Aerodynamic Study of a Pusher-Propeller Aircraft Model," Tech. Rep. TP-3040, NASA, 1990.

[13] Gentry, G. L., Jr., "Effect of Pylon Wake With and Without Pylon Blowing on Propeller Thrust," Tech. Rep. TM-4162, NASA, 1990.

[14] Block, P. J. W., and Gentry, G. L., Jr., "Directivity and Trends of Noise Generated by a Propeller in a Wake," Tech. Rep. TP-2609, NASA, 1986.

[15] Schlichting, H., *Boundary-Layer Theory*, McGraw-Hill, 1960.

[16] Li, Q., Öztürk, K., Sinnige, T., Ragni, D., Eitelberg, G., Veldhuis L. L. M., and Wang, Y., "Design and Experimental Validation of Swirl-Recovery Vanes for Propeller Propulsion Systems," *AIAA Journal (accepted manuscript)*, 2018. doi:10.2514/1.J057113.

[17] Custers, L. G. M., Hoeijmakers, A. H. W., and Harris, A. E., "Rotating shaft balance for measurement of total propeller force and moment," *15th International Congress on Instrumentation in Aerospace Simulation Facilities*, 1993. doi:10.1109/ICIASF.1993.687650.

[18] ANSYS® Academic Research Release 16.0, "Help System, Fluent," ANSYS, Inc.

[19] Stokkermans, T. C. A., van Arnhem, N., Sinnige, T. and Veldhuis, L. L. M., "Validation and Comparison of RANS Propeller Modeling Methods for Tip-Mounted Applications," *AIAA Journal*, 2018. doi:10.2514/1.J057398.

[20] Spalart, P. R., and Rumsey, C. L., "Effective Inflow Conditions for Turbulence Models in Aerodynamic Calculations," *AIAA Journal*, Vol. 45, No. 10, 2007, p. 2544–2553. doi:10.2514/1.29373.

[21] Eça, L., and Hoekstra, M., "Discretization Uncertainty Estimation Based on a Least Squares Version of the Grid Convergence Index," *Proceedings of the Second Workshop on CFD Uncertainty Analysis*, 2006.

[22] Bass, R. M., "Small Scale Wind Tunnel Testing of Model Propellers," *AIAA 24th Aerospace Sciences Meeting*, 1986. doi:10.2514/6.1986-392.

[23] Stokkermans, T. C. A., van Arnhem, N., Sinnige, T. and Veldhuis, L. L. M., "Validation and Comparison of RANS Propeller Modeling Methods for Tip-Mounted Applications," *AIAA Science and Technology Forum and Exposition*, 2018.

[24] Martinez, R., "Predictions of Unsteady Wing and Pylon Forces Caused by Propeller Installation," Tech. Rep. CR-178298, NASA, 1987.

[25] Silverstein, A., and Joyner, U. T., "Experimental Verification of the Theory of Oscillating Airfoils," Tech. Rep. TR-673, NACA, 1939.

[26] Chao, M. A. and Zhaoguang, T. A. N., "A conceptual analysis of an aircraft with rear-mounted open rotor engines," *30th ICAS Congress*, 2016.

[27] Marcus, E. A., de Vries, R., Kulkarni, A. R., and Veldhuis, L. L. M., "Aerodynamic Investigation of an Over-the-Wing Propeller for Distributed Propulsion," *Aerospace Sciences Meeting*, 2018. doi:10.2514/6.2018-2053.

[28] van Arnhem, N., Sinnige, T., Stokkermans, T. C. A., Eitelberg, G., and Veldhuis, L. L. M., "Aerodynamic Interaction Effects of Tip-Mounted Propellers Installed on the Horizontal Tailplane," *AIAA Aerospace Sciences Meeting*, 2018. doi:10.2514/6.2018-0542.

[29] Stokkermans, T. C. A., van Arnhem, N., and Veldhuis, L. L. M., "Mitigation of propeller kinetic energy losses with boundary layer ingestion and swirl recovery vanes," *RAeS Applied Aerodynamics Conference*, 2016.

[30] de Young, J., "Propellers at high incidence," *Journal of Aircraft*, Vol. 23, No. 3, 1965, pp. 241–250. doi:10.2514/3.43646.

This article has been cited by:

1. Mojtaba Tahani, Mehran Masdari, Ali Bargestan. 2021. Aerodynamic ground effects on DLRF6 vehicle. *Aircraft Engineering and Aerospace Technology* **93**:5, 755-767. [Crossref]
2. Hugo F. Bento, Reynard de Vries, Leo L. Veldhuis. Aerodynamic Performance and Interaction Effects of Circular and Square Ducted Propellers . [Abstract] [PDF] [PDF Plus]
3. Maurice Hoogreef, Reynard de Vries, Tomas Sinnige, Roelof Vos. Synthesis of Aero-Propulsive Interaction Studies Applied to Conceptual Hybrid-Electric Aircraft Design . [Abstract] [PDF] [PDF Plus]
4. Reynard de Vries, Nando van Arnhem, Francesco Avallone, Daniele Ragni, Roelof Vos, Georg Eitelberg, Leo L. Veldhuis. Aerodynamic Interaction Between an Over-the-Wing Propeller and the Wing Boundary-Layer in Adverse Pressure Gradients . [Citation] [PDF] [PDF Plus]
5. Nando van Arnhem, Reynard de Vries, Roelof Vos, Leo L. Veldhuis. Aerodynamic Performance of an Aircraft Equipped with Horizontal Tail Mounted Propellers . [Citation] [PDF] [PDF Plus]